

Document downloaded from:

<http://hdl.handle.net/10251/62309>

This paper must be cited as:

Lopez Martinez, JA.; Serna Ros, P.; Juan Navarro-Gregori; Camacho Torregrosa, EE. (2015). An inverse analysis method based on deflection to curvature transformation to determine the tensile properties of UHPFRC. *Materials and Structures*. 48(11):3703-3718. doi:10.1617/s11527-0.14-0.434-0.



The final publication is available at

<https://doi.org/10.1617/s11527-014-0434-0> (see policy)

Copyright Springer Verlag (Germany)

Additional Information

# AN INVERSE ANALYSIS METHOD BASED ON DEFLECTION TO CURVATURE TRANSFORMATION TO DETERMINE THE TENSILE PROPERTIES OF UHPFRC

## FIRST / CORRESPONDING AUTHOR

Juan Ángel López

PhD Student

Universitat Politècnica de València

[jualoma7@gmail.com](mailto:jualoma7@gmail.com)

+34 605 670 422

## CO-AUTHORS

Pedro Serna

University Professor

Universitat Politècnica de

València

[pserna@cst.upv.es](mailto:pserna@cst.upv.es)

Juan Navarro-Gregori

Assistant Professor

Universitat Politècnica de

València

[juanagre@cst.upv.es](mailto:juanagre@cst.upv.es)

Esteban Camacho

Dr. Civil Engineer

Universitat Politècnica de

València

[estebancamacho@msn.com](mailto:estebancamacho@msn.com)

## 1.- INTRODUCTION

Ultra-High Performance Fibre-Reinforced Concrete (UHPFRC) is defined as a cement-based composite material, which combines three technical advances in concrete: (1) high compressive strength of more than 150 MPa; (2) ductile behaviour under tension due to the presence of steel fibres, which can provide a pseudo strain-hardening stress-strain response accompanied by multiple cracking in accordance with the fibres volumetric ratio, isotropic distribution or favourable orientation ; (3) a special selection of fine and ultrafine aggregates that provides dense particle packing, high durability and flowability (SETRA-AFGC, 2002) (AFGC,2013).

The way to achieve over 200 MPa has been known since 1981 (Bache, 1981); using low water binder ratios, a large quantity of superplasticizer and ultrafine particles. Besides, UHPFRC can be considered a special type of High Performance Fibre Reinforced Cement Composites (HPFRCC) if the definition found in the Preface of the 6<sup>th</sup> Symposium on HPFRCC (Parra-Montesinos, et al., 2011) and (JSCE, 2008) is used. Naaman introduced this concept in 1987 (Naaman, 1987). In 1994, the term Ultra-High Performance Concrete (UHPC) was first used (de Larrard & Sedran, 1994) to refer to an optimised particle-packing material. Therefore, the innovation of UHPFRC lies in the integration of all of these technologies into only one material.

Although the technologies on which UHPFRC are based have been long since well-known, the determination of its tensile properties is still a challenge to researchers. Some authors have used a traditional load-CMOD diagram to obtain the  $\sigma$ - $\epsilon$  response in a standardised notched three-point bending test based on RILEM TC162-TDF (EN-14651). However, since these recommendations focus on traditional strength concretes of up to 80 MPa with a lower fibre content than 80 kg/m<sup>3</sup> (Walraven, 2012), they do not seem to be adequate for UHPFRC. In UHPFRC, the larger amount of fibres ensures a non-brittle behaviour after matrix cracking. In those cases where UHPFRC exhibits pseudo-strain hardening

behaviour with great strain capacity before the crack localisation, the consideration of a stress-strain approach can be more appropriate than a stress crack-opening approach (Baby, et al., 2012).

The tensile properties of structural UHPFRC elements must be established in two different steps. In the first one, representative specimens of the structural elements must be chosen. Thus, its size and also its way of casting must be carefully selected to avoid scale effects, and it is necessary to ensure that fibres orientation and distribution are similar to the structural elements (1D, 2D or 3D) (Tailhan, et al., 2004) (SETRA-AFGC, 2002). After selecting the specimens, a suitable test must be run in a second step. The uniaxial tensile test (UTT) is considered complicated because it is very sensitive to several factors, such as specimen imperfections, loading machine stiffness, shrinkage, boundary conditions, stress concentrations at the fixation points or the non-uniformity of the material itself (Kanakubo, 2006) (Qian & Li, 2007) (Ostergaard, et al., 2005). Even though some recent works have been performed to develop suitable, easy-to-conduct UTT (Reineck & Frettlöhr, 2010) (Graybeal & Baby, 2013), the unnotched four-point bending test (FPBT) offers a simpler alternative to UTT and has already been used by several authors to determine the tensile behaviour of UHPFRC. Thus, the inverse analysis consists in determining the  $\sigma$ - $\varepsilon$  response from the results obtained in the FPBT.

Several methods have been proposed to carry out the inverse analysis. The different methods proposed have a point in common: they attempt to reproduce the experimental measurements by means of more or less complex models which directly depend on the uniaxial tensile and compressive parameters. These methods can be sorted into two main groups: methods based on the experimental key points taken from test, called simplified methods; and methods based on a complete experimental law. The latter can be also classified, according to how the parameters adjustment is made, in the iterative methods and point-by-point methods. Iterative methods assume a constitutive law in both compression and tension. During the iterative process, these parameters are modified to minimise the error between the model proposed and the experimental results. Point-by-point methods build the constitutive law progressively in each loading step. This process leads to a rough constitutive law, which requires a post-process for its easy implementation and use.

Simplified methods take only a few specific points from the results obtained during the FPBT. These points are usually modulus of rupture (*MOR*) and loss of linearity point, which is not clearly defined for UHPFRC. These are the methods proposed in (SETRA-AFGC, 2002), (AFGC, 2013) and (Kanakubo, 2006). Despite these methods being easy to implement, they offer a poor approach.

The methods based on a complete experimental law use load-deflection, the load-strain at the tension face, or the load-average curvature between load points to reproduce the test and to adjust the uniaxial tensile and compressive parameters. These methods can be sorted according to the above-mentioned experimental laws used for the adjustment.

Load-deflection methods are more common and intuitive, and they determine the tensile parameters by comparing between the load-deflection experimental curve and the analytical curve proposed. The theoretical load-deflection curve is obtained by more or less complex FEM models. The main problem of these methods lies in the hypothesis needed to obtain deflection during the descending branch. However, many authors are satisfied by working only with the loading branch, which cannot be right. Thailand et al. (Tailhan, et al., 2004) proposed a 2D FEM model with a displacement formulation without considering any hypothesis for the unloading branch. Both Ostergaard et al. (Ostergaard, et al., 2005) and Soranakom et al. (Soranakom & Mobasher, 2007) proposed a model which takes it into account; therefore, the softening parameters of the tensile constitutive law can be determined. The former proposed a hinge model, which considered the position of the crack and the hinge. The latter suggested a method based on a close-form formulation for moment-curvature relationships based on a trilinear assumption of the tensile  $\sigma$ - $\varepsilon$  law (Soranakom & Mobasher, 2008). After maximum load, this model assumes a damage area length to reproduce the unloading branch.

1 The load-strain method was recently developed in (Baby, et al., 2012). This method requires the measurement of the  
2 average strain at the tension face between the applied loads. For each load-strain experimental measure, a mechanical  
3 equilibrium in the central section is done to determine the tensile stress-strain law by means of a point-by-point process.  
4 A linear law in compression is used given the high compression strength of UHPFRC. This process leads to a rough  
5 constitutive law in tension, which has to be transformed. Hence, this method requires a post-process above the initial  
6 constitutive law obtained.  
7

8  
9 In the load-curvature method, measured deflection is converted into an average curvature between applied load points  
10 by an equation that relates these two variables. In (Rigaud, et al., 2011), an equation is used which is based on the  
11 assumption of a linear curvature distribution between the supports and the applied load points. A similar point-by-point  
12 process to (Baby, et al., 2012) is used after the transformation to establish the tensile parameters. In (Qian & Li, 2007),  
13 another equation is suggested which is based on structural elastics mechanics and takes into account the influence of  
14 shear, but it is less successful. In both cases, these hypotheses underestimate the curvature (Baby, et al., 2012). In  
15 (Baby, et al., 2013), an iterative displacement to curvature transformation based on the double integration of the  
16 curvature over the length of the prism specimen is proposed. In a second step, a point-by-point process similar to (Baby,  
17 et al., 2012) and (Rigaud, et al., 2011) is employed.  
18  
19  
20  
21  
22

23 The widespread use of UHPFRC requires a simple, reliable method to determine its tensile constitutive law. If a more  
24 approximate equation that relates the mid-span deflection and curvature, and an analytical moment-curvature close-form  
25 formulation adapted to UHPFRC, could be developed, the back-analysis would be easy, quick, and reliable.  
26  
27

## 28 2.- SCOPE AND OBJECTIVES 29 30

31 The main objective of this work is the development and validation of a new inverse analysis methodology based on a  
32 load-curvature method which improves both the (Rigaud, et al., 2011) and (Qian & Li, 2007) methods. First of all, a  
33 method for transforming mid-span deflection into an average curvature in a FPBT is developed. Having obtained the  
34 experimental bending moment versus the curvature law from the load-deflection FPBT data, an analytical moment-  
35 curvature close-form formulation based on (Soranakom & Mobasher, 2007) and adapted for UHPFRC is developed to  
36 obtain the tensile  $\sigma$ - $\varepsilon$  parameters which best fit UHPFRC behaviour in the region between the applied load points. This is  
37 achieved by means of an iterative process which focuses on minimising the error between both the experimental and  
38 analytical curves by varying the constitutive tensile parameters.  
39  
40  
41  
42

43 The deflection to average curvature transformation method has been validated by means of a theoretical analysis.  
44 Besides, the four-point bending tests performed in (Kanakubo, 2006), in which both the deflection and average  
45 curvatures at mid-span are measured for the UHPFRC specimens, were used to validate the suggested transformation.  
46 The deflection to curvature methods proposed in (Rigaud, et al., 2011) and (Qian & Li, 2007) were also compared with  
47 the experimental data.  
48  
49  
50

51 Finally, an inverse analysis over bending tests performed in (Tailhan, et al., 2012) was carried out to provide an  
52 application example of how the new methodology works and to compare the results to those obtained in (Tailhan, et al.,  
53 2012).  
54  
55  
56

## 57 3.- PROPOSED INVERSE ANALYSIS BASIS 58

### 59 3.1.- Close-form bending moment – curvature ( $M$ - $\Phi$ ) formulation 60 61 62 63 64 65

The bending moment versus the curvature relationship is deduced from a simplified  $\sigma$ - $\varepsilon$  relationship developed on the basis of a number of assumptions in both compression and tension. It is known that in compression, UHPFRC is considered to remain linear-elastic by up to 70-80% of the maximum load (Spasojevic, 2008). Depending on its compressive strength, UHPFRC compressive behaviour can be considered linear-elastic up to strain levels of between 2-3‰ (Graybeal, 2006). The model developed in this work assumes linear behaviour for any strain value as in (Baby, et al., 2012). Although this hypothesis may induce error at a high compressive strain level, it allows the development of formulation which dispenses with any compressive parameter. A trilinear  $\sigma$ - $\varepsilon$  relationship in tension has been considered to define UHPFRC behaviour in pure tension. Although the UTT results provide a non-linear  $\sigma$ - $\varepsilon$  relationship during softening (Graybeal, 2006) (Wille, et al., 2014), a linear approach may be adequate to reduce the number of parameters required to define the material model in tension.

Figure 1 shows the constitutive  $\sigma$ - $\varepsilon$  law used in this work, along with the notation and the five parameters used to model UHPFRC behaviour. Elastic modulus  $E$  is considered the same in both compression and tension. The other four parameters which complete the tensile law are: first cracking tensile stress  $f_t$ , ultimate tensile strength  $f_{t,u}$ , its associated strain  $\varepsilon_{t,u}$ , and maximum strain  $\varepsilon_{t,max}$ . The strain at the end of the linear stage  $\varepsilon_{t,el}$ , can be expressed as the relation between  $f_t$  and  $E$ .

Using the constitutive hypothesis shown in Figure 1, four different stages in accordance with the strain at the most tension fibre can be distinguished: linear elastic up to the matrix-cracking strain,  $\varepsilon_{t,el}$ , (Stage I); the pseudo-strain hardening behaviour characterised by multiple micro-cracking up to crack localisation,  $\varepsilon_{t,u}$ , (Stage II); the softening behaviour characterised by the development of the macro crack up to fibre debonding,  $\varepsilon_{t,max}$ , (Stage III); and the fibre debonding stage (Stage IV). If the  $f_{t,u}$  value is defined to be lower than  $f_t$ , both Stage II and Stage III correspond to softening behaviour.

Figure 1. The  $\sigma$ - $\varepsilon$  law in both compression and tension. Cross-sectional stress distribution for the different stages.

To simplify the formulation, three normalised parameters were introduced:  $\alpha$ ,  $\beta$  and  $\gamma$ , defined in Equation (1).

$$\varepsilon_t = \frac{f_t}{E}; \quad \alpha = \frac{\varepsilon_{t,u}}{\varepsilon_t}; \quad \beta = \frac{\varepsilon_{t,max}}{\varepsilon_t}; \quad \gamma = \frac{f_{t,u}}{f_t} \quad (Eq. 1)$$

Following the steps pointed out in (Soranakom & Mobasher, 2007), the moment-curvature relationship can be obtained for the four stages (Figure 1). By considering a non-reinforced rectangular  $b \times h$  cross-section with null axial force under the assumption that plane sections remain plane, the close-form  $M$ - $\Phi$  formulation was obtained using the  $\sigma$ - $\varepsilon$  law in Figure 1. For each stage, the axial force and the bending moment can be expressed according to the constitutive law parameters and the two additional parameters. For this work, these two parameters were the curvature and the strain at the tension face,  $\varepsilon_f$  (Figure 1). Using the axial force equation and the null axial force condition in the section, the strain at the tension face can be expressed according to the curvature for each stage. By substituting this expression in the bending moment equation, it is possible to obtain the  $M$ - $\Phi$  relationship in accordance with the constitutive parameters. In Table 1, the  $M$ - $\Phi$  for the different stages is shown. Parameters  $\Phi_{el}$ ,  $\Phi_h$  and  $\Phi_s$  in Table 1 correspond to the curvature in which the strain at the most tension fibre is  $\varepsilon_{t,el}$ ,  $\varepsilon_{t,u}$  and  $\varepsilon_{t,max}$ , respectively.

Table 1. The close form  $M$ - $\Phi$  formulation suggested for a UHPFRC rectangular cross-sectional shape

Figure 2 shows the normalised M-  $\Phi$  curve for typical UHPFRC using the equations in Table 1 for Stages I to III. Stage IV is not represented to be able to better appreciate behaviour until the maximum load. Parameter  $\sigma_{fl}$  was obtained using Equation (2) (Figure 3).

$$\sigma_{fl} = \frac{6M}{bh^2} = \frac{3Pa}{bh^2} \quad (Eq. 2)$$

This curve remains analogous if another kind of UHPFRC is used with other constitutive parameters. As can also be seen, the three curves are continuous and the same slope remains at the intersection point. Interestingly, it can be clearly observed that the matrix cracking tensile stress,  $f_t$ , is reached before sufficient loss of significant linearity takes place to be detected. In fibre-reinforced concrete, significant loss of linearity is established by the limit of proportionality in EN-14651. However, loss of linearity is not clearly defined for the UHPFRC. A correct definition of this point may be of interest to determine the first cracking tensile stress from this point. As Figure 2 illustrates, the difference between cracking tensile stress and apparent loss of linearity is due to the shape of the hardening curve. Based on these equations, and having properly defined loss of the linearity point, it would be possible to determine the theoretical coefficient that relates these two values.

When the UHPFRC exhibits hardening behaviour in bending, which is very common for this material, the maximum bearing moment capacity is always reached after macro-crack formation (Figs. 1 and 2). Thus, the maximum bending moment is reached with a higher strain at the most tension fibre than that corresponding to maximum tensile stress; that is, after the crack localisation takes place in either Stage III for pseudo-hardening behaviour in tension, or Stage II for softening behaviour in tension. This fact is in agreement with (Baby, et al., 2012) and confers much importance to the softening branch.

Figure 2. Normalised moment-curvature curve for typical UHPFRC with a rectangular cross-section.  $f_t = 9 \text{ MPa}$ ;  $f_{t,u} = 10 \text{ MPa}$ ;  $\varepsilon_{t,u} = 0.25\%$ ;  $\varepsilon_{t,max} = 3.4\%$ ;  $E=50 \text{ GPa}$ ;  $b=h=0.1 \text{ m}$ .

### 3.2.- Deflection at the mid-span to average curvature transformation ( $\delta$ to $\Phi$ transformation)

The deflection to curvature transformation method developed in this work is in agreement with the FPBT. The  $\delta$ - $\Phi$  relationship at mid-span is established by means of Timoshenko equations (Eq. 3). By considering a non-linear curvature distribution, the non-linearity in bending is taken into account. Shear deflection can be large enough to not be neglected, but depends on the specimen height and the shear span of the test (Graybeal, 2006). The use of Equation (3) implies that shear stiffness remains constant in all the tests. This fact can be assumed since no shear cracking was pointed out by any of the authors during FPBT in UHPFRC for common spans and heights. By considering a Poisson's ratio of 0.2 (SETRA-AFGC, 2002) and a shear area of  $5bh/6$ , in line with the Timoshenko theory, the Timoshenko expression for the FPBT leads to Equation (4).

$$\delta = \frac{L}{2} \int_0^{L/2} \phi(x) dx - \int_0^{L/2} \phi(x) \left[ \frac{L}{2} - x \right] dx + \frac{1}{GA} \int Q(x) dx \quad (Eq. 3)$$

$$\delta = \frac{L}{2} \int_0^{L/2} \phi(x) dx - \int_0^{L/2} \phi(x) \left[ \frac{L}{2} - x \right] dx + \frac{36Pa}{25Ebh} \quad (Eq. 4)$$

This method requires a curvature distribution hypothesis along the beam in accordance with the load applied. Although the theoretical  $M(\Phi)$  relationship has already been obtained (Table 1), the inverse relation  $\Phi(M)$  is very difficult to obtain, and the resulting equations can be very complicated for being analytically integrated to obtain the  $\Phi-\delta$  relationship. For this reason, it is necessary to assume a  $\Phi(x)$  distribution which has to be easy-integrated and must approximate the theoretical relationship.

The easiest procedure consists in assuming a linear curvature distribution in Zone 2 (Figure 3) and a constant one in Zone 1 (Figure 3). This hypothesis is consistent with the FPBT since this is the real curvature distribution expected in the FPBT in the linear stage. Equation (5) shows this hypothesis.

$$\phi(x) = \begin{cases} \frac{\bar{\phi} x}{a} & \text{if } x \leq a \\ \bar{\phi} & \text{if } a < x \leq L/2 \end{cases} \quad (\text{Eq. 5})$$

Parameter  $\bar{\phi}$  represents the average curvature in Zone 1. Before crack localisation, the average curvature is the same as the curvature at each point inside Zone 1 (Figure 3). However after crack localisation has taken place, it is easier to deal with an average curvature. According to this assumption, the disturbed cracked section is considered to be smeared over Zone 1, which quite often coincides with specimen depth.

The linear approach provides an exact solution up to the matrix cracking tensile stress. In addition for load levels of up to approximately 70% of maximal flexural load, curvatures deviate slightly from the elastic curvatures (Spasojevic, 2088) given the insignificant loss of linearity (Figure 2). However, this method greatly underestimates the curvature over this value for a given displacement at mid-span (Baby et al., 2013). Figure 3 illustrates how this hypothesis works. In a first step, when the applied load is lower than the first cracking load, this assumption is absolutely certain. In a second step with an applied load of about 70% of the maximum bearing capacity, the curvature is slightly underestimated at Zone 1 due to an overestimation in Zone 2 (Figure 3). At this point, it is necessary to remark that both the curvature distributions shown in Figure 3 correspond to the same applied load and the same displacement at mid-span as we are looking for the curvature which is in correspondence with the displacement measure at mid-span for each loading step. In a third step, as load increases, the underestimation of the curvature for the same displacement also increases. In Figure 3,  $\Phi_i$  and  $\Phi_{i,linear}$  represent the curvature distribution expected in a FPBT and the curvature obtained using the linear approach.

Figure 3. Qualitative comparison between the real curvature distribution and the linear approach for different loading steps

In order to improve the linear assumption, it is necessary to develop a new hypothesis. Since the curvature law increases quickly close to the maximum load, a natural logarithm curve (Eq. 6) was used. This curve has been defined so that its initial slope corresponds with the slope of the linear-elastic beams theory for each loading step.

$$\phi(x) = \begin{cases} -\frac{6Pa}{Eb^3h^3} \ln\left(1 - \frac{x}{a}\right) & x < a \\ \bar{\phi} & a \leq x \leq L/2 \end{cases} \quad (\text{Eq. 6})$$

By replacing Equations (5) and (6) in Equation (4),  $\delta-\Phi$  can be easily obtained. The results are shown in Equation (7) and Equation (8) for the linear and the logarithm approach, respectively.

$$\delta = \frac{\bar{\phi}}{24} [3L^2 - 4a^2] + \frac{36Pa}{25Ebh} \quad (Eq. 7)$$

$$\delta = \frac{\bar{\phi}}{8} [L^2 - 4a^2] + \frac{9Pa^3}{2Ebh^3} + \frac{36Pa}{25Ebh} \quad (Eq. 8)$$

The equation which allows us to obtain the average curvature in Zone 1 from the deflection measured at mid-span is easily derived from Equations (7) and (8). Equations (9) and (10) show the linear transformation and the logarithm transformation, respectively.

$$\bar{\phi} = \frac{24}{3L^2 - 4a^2} \left[ \delta - \frac{36Pa}{25Ebh} \right] \quad (Eq. 9)$$

$$\bar{\phi} = \frac{8}{L^2 - 4a^2} \left[ \delta - \frac{9Pa^3}{2Ebh^3} - \frac{36Pa}{25Ebh} \right] \quad (Eq. 10)$$

#### 4.- ANALYTICAL VALIDATION OF THE $\delta$ TO $\phi$ TRANSFORMATION

The FPBT is an isostatic test, so the bending moment law is defined by the equilibrium equations for every loading step. If the beam is divided into  $n$  points with a gap of  $\Delta x$  between them, the bending moment at each point can be easily determined. Using  $M-\phi$  shown in Table 1, it is possible to determine the curvature law along the beam that is associated with each applied load. After establishing the curvature law, it is possible to obtain the displacement due to the bending along the beam by the double integration of the curvature. In a first integration step, rotation angle ( $\phi$ ) is obtained using Equation (11), and by considering that the rotation angle at mid-span is null. In a second step, the displacement due to bending ( $\delta_b$ ) can be determined using Equation (12) and by considering the null displacement at the supports (Figure 4).

$$\Delta\phi = \phi \cdot \Delta x \quad (Eq. 11)$$

$$\Delta\delta_b = \phi \cdot \Delta x \quad (Eq. 12)$$

Since the shear forces may play a significant role in total displacement, it is necessary to determine it. As with bending moment distribution, shear distribution can be simply determined using the equilibrium equations. Shear rotation angle ( $\gamma$ ) is obtained using Equation (13), where  $Q$  is the shear force,  $G$  is the shear stiffness and  $A_q$  is the effective shear area. By directly integrating the rotation angle, the displacement due to shear forces ( $\delta_s$ ) can be determined using Equation (14) (Figure 4).

$$\gamma = \frac{Q}{GA_q} \quad (Eq. 13)$$

$$\Delta\delta_s = \gamma \cdot \Delta x \quad (Eq. 14)$$

Figure 4. Procedure to obtain the load-displacement load up to maximum load due to the flexural and shear forces in a FPBT



At this point, what is really interesting is the total displacement at mid-span as this is the parameter used to obtain the average curvature at Zone 1 (Eqs. (10) and (11)). The following analytical results were obtained for a prismatic specimen with a 100x100 mm square cross-section and a 450 mm span, where 150 mm is parameter  $a$  (Figure 4). Checks were also made to see if the results were similar for other common specimen sizes, such as 150x150x450, 100x100x300, 50x50x(450,300,150), 200x40x600, 40x200x600 mm, where the  $a$  parameter is one third of the span. It was also necessary to define the constitutive parameters of the material. A typical  $\sigma$ - $\varepsilon$  law in tension for UHPFRC was selected:  $f_t = 9$  MPa;  $f_{t,u} = 10$  MPa;  $\varepsilon_{t,u} = 0.25\%$ ;  $\varepsilon_{t,max} = 3.4\%$ ;  $E=50$  GPa. Similar results can be seen for other types of UHPFRC. Following the procedure, the above-described geometry and mechanical properties, and the load-deflection curve at mid-span are included in Figure 5.

Figure 5. The numerical load-deflection curve at mid-span for a prismatic 100x100x450mm FPBT.  $f_t = 9$  MPa;  $f_{t,u} = 10$  MPa;  $\varepsilon_{t,u} = 0.25\%$ ;  $\varepsilon_{t,max} = 3.4\%$ ;  $E=50$  GPa.

The load-average curvature curve is obtained from the results shown in Figure 5 and in Equations (9) and (10) for both the linear and logarithm transformation hypotheses. Besides, the theoretical  $\Phi$  at mid-span for each load step can also be obtained from the equations in Table 1. Figure 6 offers these three curves. As expected, the theoretical and linear hypotheses almost coincide by up to 70% of the bearing load. As of over 70% of the maximum load, the linear hypothesis starts to separate from the theoretical, while the logarithm hypothesis increasingly comes closer to 90% of the maximum load, when they coincide.

Figure 6. The load-average curvature at mid-span for a prismatic 100x100x450mm FPBT.  $f_t = 9$  MPa;  $f_{t,u} = 10$  MPa;  $\varepsilon_{t,u} = 0.25\%$ ;  $\varepsilon_{t,max} = 3.4\%$ ;  $E=50$  GPa.

Since the linear hypothesis offers a more accurate estimation at the beginning, and the logarithm approach does so at the end, the best choice is to sever Equation into two parts by its intersection point (Figure 5). The final  $\Phi(\delta)$  relationship proposed in this work is shown in Equation (15). Another way to define this equation, and perhaps an easier way to introduce it into a spreadsheet, is by taking the highest values obtained by the two hypotheses. This alternative form is shown in Equation (16). It can be observed that both formulations lead to the same  $\delta$  to  $\Phi$  transformation.

$$\phi(\delta) = \begin{cases} \frac{24}{3L^2 - 4a^2} \left[ \delta - \frac{36Pa}{25Ebh} \right] & \delta \leq \frac{Pa}{Ebh} \left[ \frac{36}{25} + \frac{27}{16} \left( \frac{L}{h} \right)^2 - \frac{9}{400} \left( \frac{a}{h} \right)^2 \right] \\ \frac{8}{L^2 - 4a^2} \left[ \delta - \frac{9Pa^3}{2Ebh^3} - \frac{36Pa}{25Ebh} \right] & \delta > \frac{Pa}{Ebh} \left[ \frac{36}{25} + \frac{27}{16} \left( \frac{L}{h} \right)^2 - \frac{9}{400} \left( \frac{a}{h} \right)^2 \right] \end{cases} \quad (Eq. 15)$$

$$\phi(\delta) = \max \left\{ \begin{array}{l} \frac{24}{3L^2 - 4a^2} \left[ \delta - \frac{36Pa}{25Ebh} \right] \\ \frac{8}{L^2 - 4a^2} \left[ \delta - \frac{9Pa^3}{2Ebh^3} - \frac{36Pa}{25Ebh} \right] \end{array} \right\} \quad (Eq. 16)$$

In order to understand why linear hypotheses tend to increasingly separate above 70% of the maximum load, and why the logarithm hypotheses act in the opposite way, Figure 7 was produced. In Figure 7, the curvature distribution along the half-beam length for the different loading steps is drawn; 50%, 70%, 90% and 100% of the maximum bearing capacity, both the different curvature distribution hypotheses, and the theoretical distribution given by the formulation in Table 1. For each loading step, average curvature ( $\bar{\Phi}$ ) is taken from Figure 6. Using equations (5) and (6), the curvature distribution along the beam is obtained for both the linear and logarithm hypotheses.

1 It is important to remark that the three curvature distributions along the beam offer the same displacement at mid-span  
 2 for all the load steps and that the really important parameter is the curvature at Zone 1. As expected, the linear  
 3 distribution requires a small average curvature due to an overestimation of Zone 2 (Figure 4) when the theoretical  
 4 distribution loses its linearity. Despite the logarithm hypothesis distribution not being defined at the point where the load  
 5 is applied ( $a$ ), it offers good results when load is over 70% of the maximum load due to its fast growth.  
 6  
 7

8  
 9 Figure 7. Curvature distribution along the half-length beam for several loading steps using the different hypothesis  
 10 suggested.  $f_t = 9 \text{ MPa}$ ;  $f_{t,u} = 10 \text{ MPa}$ ;  $\varepsilon_{t,u} = 0.25\%$ ;  $\varepsilon_{t,max} = 3.4\%$ ;  $E=50 \text{ GPa}$ ,  $b=0.1\text{m}$ ;  $h=0.1\text{m}$ ;  $L=0.45\text{m}$ ;  $a=0.15\text{m}$   
 11  
 12

13 Based on the results obtained in this paragraph, it can be stated that the proposed  $\delta$  to  $\Phi$  transformation is simple to use  
 14 and to implement in a spreadsheet. Although the method is analytically reliable, it is necessary to check it with  
 15 experimental results.  
 16  
 17

## 18 5.- EXPERIMENTAL VALIDATION OF THE $\delta$ TO $\Phi$ TRANSFORMATION

19  
 20  
 21 The results obtained from this new  $\delta$  to  $\Phi$  transformation were checked using the results obtained by Kanakubo  
 22 (Kanakubo, 2006). Among other aspects, Kanakubo deals with the inverse analysis problem for UHPFRC. He performs  
 23 several FPBT over 100x100x300 prismatic specimens and measures not only the displacement at mid-span, but also the  
 24 average strain at both the compressed and tensile faces (Figure 8). From the strain measures, and knowing the distance  
 25 between LVDTs, it is possible to obtain the average curvature in the central one-third (Zone 1). A comparison between  
 26 these experimental average curvature values and those obtained by the  $\delta$  to  $\Phi$  transformation was made.  
 27  
 28  
 29  
 30

31 Displacement at the mid-span should be corrected according to the position of the macrocrack before  $\delta$ - $\Phi$  transformation  
 32 to obtain better accuracy in the average curvature estimation after crack localisation (Groeger, et al., 2012). However  
 33 since no data were available, its influence for this work was neglected. Only those UHPFRC specimens in which the  
 34 macro-crack appeared inside the central one third were selected since this factor can influence the results. The selected  
 35 specimens were: BH-2, BH-3, BV-1 and BV-2 (Kanakubo, 2006).  
 36  
 37  
 38

39 Figure 8. The FPBT configuration carried out by Kanakubo (Kanakubo, 2006)  
 40  
 41

42 The deflection to curvature transformation was also done following the equations proposed by Rigaud (Rigaud, et al.,  
 43 2011) and Qian (Qian & Li, 2007). To compare each methodology, Equation (17) was used, where  $n$  is the number of  
 44 data points for each test. The comparison results are provided in Table 2.  
 45  
 46  
 47

$$48 \text{\%Deviation} = 1000 \sum_{i=1}^n \frac{(\phi_{i,exp} - \phi_{i,model})^2}{n-1} \quad (Eq. 17)$$

49  
 50  
 51 Table 2. Deviation in the curvature determination by the different load-curvature methods  
 52  
 53

54 Table 2 shows that the new proposal improves the last two methods and that it leads to theoretical values which come  
 55 closer to the experimental measures. The results of the four specimens are also provided in Figure 9. The new model  
 56 reproduces the experimental results with high precision. Most deviation is located between 70-80% of the maximum load  
 57 in the ascending branch, since neither linear distribution nor logarithm distribution is suitable. However, the new  
 58 procedure offers a better approach than the previous ones, and also in this stage. The new method works much better  
 59  
 60  
 61  
 62  
 63  
 64  
 65

than others at above 70-80% of the maximum flexural load and during the descending loading branch. Figure 9 shows that while the Rigaud and Qian methods produce a significant deviation from the experimental results, the new method reproduces the test even in the unloading branch.

Figure 9. The  $\delta$  to  $\Phi$  transformation using the Qian, Rigaud and Lopez methods and their comparison with the experimental results in the BH1, BH2, BV1 and BV2 specimens (Kanakubo, 2006)

The test results also allow the determination of the strain at the most compressed fibre using the experimental value of  $\epsilon_1$  (Figure 8) and the experimental curvature. The results showed that strain values above 2‰ are reached for the four specimens during the descending branch with loss of capacity above 10%. From this point onwards, the developed close-form formulation may induce some error in the determination of the softening tension branch.

Figure 10 depicts the comparison made between the different methods shown for the BH-2 specimen. The results reveal, as expected, that the Rigaud et al. (Rigaud, et al., 2011) and Qian et al. (Qian & Li, 2007) methods underestimate the curvature value at high level loads because of the linear approach they assumed. However despite using a linear hypothesis, the curvature in the elastic stage is overestimated in these methods. The only difference between Rigaud method (Rigaud, et al., 2011), which has been developed in this work in the linear phase, is the consideration of shear deflection. Depending on its size, it may significantly influence specimen behaviour (Graybeal, 2006).

In the linear elastic phase, the elastic modulus can be easily obtained for an FPBT using Equation (18). It has been considered that  $a = L/3$ , which is common in FPBT. According to this hypothesis, the curvature in the linear elastic phase can be deduced from Equation (9). Equations (19) and (20) show the curvature at the mid-span in the linear elastic phase with and without considering shear deflection, respectively.

$$E = \frac{M}{I\phi} = \frac{2PL}{\phi bh^3} \quad (Eq. 18)$$

$$\phi_{with\_shear} = \frac{216}{23L^2} \left( \delta - \frac{72PL}{150Ebh} \right) \quad (Eq. 19)$$

$$\phi_{without\_shear} = \frac{216\delta}{23L^2} \quad (Eq. 20)$$

By substituting Equations (19) and (20) in Equation (18), the relationship between the elastic modulus obtained with and without considering shear deflection can be obtained. This relationship is shown in Equation (21). In these tests the relation  $h / L$  is 1/3, which becomes an error of 20% in the elastic modulus estimation if no shear deflection is considered. The analytical results agree with the experimental results shown in Figure 10. Therefore, by taking into account the shear deflection, it is essential to well calibrate the model, especially the elastic modulus and first cracking tensile stress.

$$\frac{E_{with\_shear}}{E_{without\_shear}} = 1 + 2.254 \left( \frac{h}{L} \right)^2 \quad (Eq. 21)$$

Figure 10. The comparison made of the Qian, Rigaud and Lopez methods with the experimental results for the BH-2 specimen.

1 The new proposed methodology improves the existing  $\delta$  to  $\Phi$  transformation methods, and also offers a very good  
2 approach to the measures taken within Zone 1. Thus, by means of this transformation, it is not necessary to measure the  
3 average curvature every time a FPBT is done, which is sometimes hard to perform, since the proposed methodology can  
4 reproduce it with high accuracy from the easy deflection at mid-span measure. Note that its accuracy has been checked  
5 only with the deflection-hardening specimens.  
6

## 7 8 6.- APPLICATION EXAMPLE OF THE PROPOSED INVERSE METHOD OVER TAILHAN'S (Tailhan, et al., 9 2012) FPBT 10

### 11 12 6.1 Methodology 13

14  
15 With the close-form  $M-\Phi$  formulation developed in this work, and with the  $\delta$  to  $\Phi$  transformation suggested, the inverse  
16 analysis of an FPBT is easy and quick. For each couple point  $P-\delta$  of the FPBT, the  $\delta$  to  $\Phi$  transformation in Equation (16)  
17 is applied to obtain the  $P-\Phi$  experimental curve. It is common to use the equivalent flexural strength,  $\sigma_{\eta}$ , instead of the  
18 applied load or the moment at mid-span. The transformations used are shown in Equation (2) for a rectangular cross-  
19 section.  
20  
21

22  
23 Simultaneously, every curvature value obtained in the  $\delta$  to  $\Phi$  transformation is introduced into the equations in Table 1.  
24 Thus, the moment versus curvature analytical law is obtained. By means of Equation (2), the bending moment can be  
25 converted into equivalent flexural stress, and both experimental and analytical  $\sigma_{\eta}-\Phi$  can be compared. Note that the  
26 analytical curve depends on the constitutive tensile parameters. Besides, for every  $\Phi$  point, we have only one  $\sigma_{\eta}$  point  
27 for both the experimental and analytical curves. Thus, the analytical curve was adjusted to the experimental curve,  
28 varying the constitutive parameters, in order to achieve minimal the sum of the residual squares of the  $\sigma_{\eta}$  for each  
29 curvature value. The modified constitutive parameters are: elastic modulus  $E$ ; first cracking tensile stress  $f_t$ ; ultimate  
30 tensile strength  $f_{t,u}$ ; its associated strain  $\varepsilon_{t,u}$ ; and maximum strain  $\varepsilon_{t,max}$ . Since the  $\sigma_{\eta}-\Phi$  relationship is analytical, the  
31 iterative process is truly effective and fast. The Excel SOLVER tool was used for this very purpose. At the end of the  
32 process, the  $\sigma-\varepsilon$  law parameters, including the softening branch, were obtained. The inverse analysis procedure is  
33 summarised in Figure 11.  
34  
35  
36  
37  
38  
39

40 Figure 11. Scheme of the inverse analysis procedure  
41

### 42 43 6.2 Applicability of the method 44

45  
46 Softening behaviour should be based on a fracture mechanics approach given the discrete macro-crack formation.  
47 Therefore, the tensile law should be defined in terms of stress versus crack-opening displacement. For simplicity  
48 reasons, this relationship can be smeared over a crack band width into a stress versus strain relationship. As previously  
49 described in Paragraph 4, the displacement to the curvature transformation gives the average curvature at the central  
50 one-third during test. It has also been checked that the average curvature obtained is in agreement with the experimental  
51 measures of the tested specimens, and also with strain values  $\varepsilon_1$  and  $\varepsilon_2$  (Figure 8). The methodology developed in this  
52 paper is based on a smeared cracking approach, where the crack band width is considered to be the central one-third  
53 length after localisation has taken place. If UHPFRC exhibits hardening in tension, the average space between cracks  
54 can be considered to be the link between strain and crack opening before crack localisation.  
55  
56  
57  
58  
59  
60  
61  
62  
63  
64  
65

1 Deflection to curvature transformation is valid even though the specimen shows low deflection hardening behaviour in  
2 bending, which would lead to softening behaviour in tension (Figure 9, BV1). This transformation should be limited to  
3 deflection hardening behaviour in bending because its suitability for deflection softening specimens has not been  
4 checked.

5 Even though the specimens exhibit deflection hardening behaviour in bending, the  $\sigma$ - $\varepsilon$  relationship describing its  
6 behaviour in tension does not have to (Walraven, 2012). In such cases, the close-form formulation has been already  
7 adapted to describe softening  $\sigma$ - $\varepsilon$  relationships in tension.  
8  
9

### 10 6.3 Application example 11

12 A simple example of the inverse analysis procedure has been made with the FPBT  $P$ - $\delta$  results found in (Tailhan, et al.,  
13 2012). In this work, an inverse analysis using a 2D FEM model was carried out with 600 mm length, 200 mm width and  
14 40 mm thickness specimens. Tests were performed with a 420 mm span length and with 140 mm between applied loads.  
15 The procedure illustrated in Figure 11 has been followed. Of the nine FPBT performed the average  $\sigma_{fl}$ - $\delta$  was obtained,  
16 and it is shown in Figure 12 (a). At this point, Equation (16) is applied for every displacement value. Figure 12 (b) shows  
17 this transformation. Thus, the experimental  $\sigma_{fl}$ - $\Phi$  curve is obtained.  
18  
19  
20  
21  
22

23 Figure 12. a) Average  $\sigma_{fl}$ - $\delta$  b) The  $\delta$  to  $\Phi$  transformation for the FPBT in (Tailhan, et al., 2012)  
24  
25

26 The analytical  $\sigma_{fl}$ - $\Phi$  curve is obtained by entering the curvature values into the equations in Table 1. The constitutive  
27 parameters are changed in an iterative process by minimising the sum of the residual squares. This process was  
28 followed by the Excel SOLVER tool. This tool needs given constitutive parameters to start and they can be whatsoever.  
29 After considering the initial parameters, the intermediate step and the final parameters of the adjustment process are  
30 provided in Figure 13. This adjustment process takes only a few seconds and is a very good approach to the  
31 experimental curve  
32  
33  
34  
35

36 Figure 13. The inverse analysis results for the initial, an intermediate iteration  
37  
38

39 The results obtained by Thailand et al (Tailhan, et al., 2012) can now be compared with the results given by the inverse  
40 analysis method proposed. The  $\sigma$ - $\varepsilon$  laws obtained from the inverse analysis method developed herein and in (Tailhan, et  
41 al., 2004) are compared with those obtained from experimental uniaxial tensile test (UTT) (Tailhan, et al., 2012) in Figure  
42 14. The tensile law obtained by the inverse analysis is very similar to that obtained by Thailand et al. (Tailhan, et al.,  
43 2012) when using their own methodology, but differs from the UTT tests. However, this does not mean that both inverse  
44 analysis procedures are not suitable. The high tensile values obtained for this type of UHPFRC are in correspondence  
45 with the large amount of steel fibres used, of about 11% in volume and 5.5 times higher than in conventional UHPFRC.  
46  
47  
48

49 Figure 14. The constitutive tensile law from the inverse analysis  
50  
51

### 52 6.4 Validation of the inverse analysis methodology 53

54 During the FPBT in (Tailhan, et al., 2012), some remarks include: the strain at maximum load measured at the bottom  
55 fibre is  $5 \cdot 10^{-3}$ ; cracking starts at 60% of maximum load; crack localisation takes place at the peak. With the  $\sigma$ - $\varepsilon$  law  
56 obtained from the inverse analysis, the maximum strain at the maximum load in the most tension fibre is  $5.2 \cdot 10^{-3}$ . Note  
57 that the relation between the strain at most tension fibre and the curvature was already obtained when the axial force  
58 equation and the null axial force condition in the section were imposed to determine the close-form  $M$ - $\Phi$  relationship.  
59  
60  
61  
62  
63  
64  
65

Besides, if the normalised moment-curvature relationship is represented using the  $\sigma$ - $\epsilon$  tensile law obtained (Figure 15), visual loss of linearity seems to start close to 60% of the maximal flexural load. This is the point where cracking can be firstly detected. In addition, crack localisation takes place when the softening branch in tension is reached and a macro-crack starts to develop in a section. Figure 15 shows that this point is reached just before the peak, as previously pointed out.

Figure 15. The normalised moment-curvature curve for the inverse analysis  $\sigma$ - $\epsilon$  law

All of these results are consistent with the measures taken during the FPBT. However, the tensile law differs from the UTT results. Therefore, the differences between UTT and the inverse analysis should be found out in other factors that are not associated with the inverse analysis methodology because the inverse analysis results reproduce what really happens in the FPBT. It can be concluded that, despite there being a general comparison trend between the UTT and the  $\sigma$ - $\epsilon$  law from the inverse analysis to validate the back-analysis procedure, what is really important for validation is to ensure that the inverse analysis methodology reproduced all the measures taken from the test. Therefore, the higher or lower correspondence between the UTT and the back-analysis results lies in several factors, which are found beyond the inverse analysis, such as specimen size, way of casting and fibre distribution.

## 7.- CONCLUSIONS

The inverse analysis methodology proposed herein offers a  $\sigma$ - $\epsilon$  tensile law approach that is consistent with all the parameters that can be measured in an FPBT in the central one-third; such as, curvature, strain at the most tensioned fibre, cracking start and cracking localisation. It also improves previous load-curvature methods by means of a new and reliable  $\delta$  to  $\Phi$  transformation, which predicts curvature with a higher degree of accuracy, even at the descending branch. This method is quick and easy to implement, only needs the load-deflection results of an FPBT as input, and does not require a post-process treatment. Use of this method needs to be limited to deflection-hardening specimens. The proposed simplified close-form M- $\Phi$  formulation can also be used to describe softening behaviour under pure tension if low deflection hardening behaviour is seen. Nevertheless, the obtained stress-strain relation is valid only for a given specimen height and gauge length.

## ACKNOWLEDGEMENTS

This work forms part of the "FIBAC" and "FISNE" research projects, with reference BIA2009-12722 and BIA2012-35776, respectively, supported by the Spanish Ministry of Economy and Competiveness and the FEDER fund. Support for this project is gratefully acknowledged. We also wish to thank the Universitat Politècnica de València for its Excellence Scholarship (PAID-09-11), the Spanish Ministry of Education, Culture and Sport for its FPU scholarship programme, and also Mr. Toshiyuki Kanakubo for his friendly treatment and help.

## REFERENCES

- AFGC, 2013. Ultra High Performance Fiber Reinforced Concretes. Recommendations.
- Baby, F., Graybeal, B., Marchand, and P. Toutlemonde, F., 2012. Proposed Flexural Test Method and Associated Inverse Analysis for Ultra High Performance Fiber Reinforced Concrete. *ACI Materials Journal*, 109(5): 545-556.
- Baby, F., Graybeal, B., Marchand, and P. Toutlemonde, F., 2013. UHPFRC tensile behaviour characterization: inverse analysis of four-point bending test results. *Materials and Structures*. Vol. (46), 1337-1354

- 1 Bache, H., 1981. Densified cement ultra-fine particle-based materials. *Second International Conference on*  
2 *Superplasticizers in Concrete*, 10-12 June.
- 3 de Larrard, F. and Sedran, T., 1994. Optimization of Ultra-High-Performance Concrete by the Use of a Packing Model.  
4 *Cement and Concrete Research*, 24(6): 997-1009.
- 5 Graybeal, B., 2006. Material Property Characterization of Ultra-High Performance Concrete. *Federal Highway*  
6 *Administration FHWA-HRT-06-103*, August.
- 7 Graybeal, B. and Baby, F., 2013. Direct Tension Test Method for UHPFRC. *ACI Materials Journal*, Vol. 110(2), pp. 177-  
8 186
- 9 Groeger, J., Tue, N.V., Wille, K., "Bending Behaviour and Variation of flexural Parameters of UHPFRC," Proceedings of  
10 Hipermat 2012, 3rd International Symposium on UHPC and Nanotechnology for High Performance Construction  
11 Materials, edited by M. Schmidt, E. Fehling, Kassel, Germany, March 7-9, 2012, pp. 419 - 426.
- 12 JSCE, 2008. Recommendations for Design and Construction of High Performance Fiber Reinforced Cement Composites  
13 with Multiple Fine Cracks (HPFRCC).
- 14 Kanakubo, T., 2006. Tensile Characteristics Evaluation Method for Ductile Fiber-Reinforced Cementitious Composites.  
15 *Journal of Advanced Concrete Technology*, 4(1): 3-17.
- 16 Naaman, A., 1987. High Performance fiber reinforced cement composites. *Proceedings of the IABSE Symposium on*  
17 *Concrete Structures for the Future*, pp. 371-376.
- 18 Ostergaard, L., Walter, R. and Olesen, J., 2005. Method for Determination of Tensile Properties of Engineered  
19 Cementitious Composites (ECC). *Proceedings of ConMar'05*.
- 20 Parra-Montesinos, G., Reinhardt, H. and Naaman, A., 2011. High Performance Fiber Reinforced Cement Composites 6  
21 (HPFRCC6). *RILEM Bookseries*.
- 22 Qian, S. and Li, V., 2007. Simplified Inverse Method for Determining the Tensile Strain Capacity of Strain Hardening  
23 Cementitious Composites. *Journal of Advanced Concrete Technology*, 5(2): 235-246.
- 24 Reineck, K.-H. and Frettlöhr, B., 2010. Test on scale effect of UHFPRC under bending and axial forces. *3<sup>RD</sup> Fib*  
25 *International Congress*. Washington DC. Paper 54, pp.40
- 26 Rigaud, S., Chanvillar, G. and Chen, J., 2011. Characterization of Bending and Tensile Behavior of Ultra-High  
27 Performance Concrete Containing Glass Fibers. *6th International Symposium on High Performance Fiber*  
28 *Reinforce Cement Composites*, pp. 373-380.
- 29 SETRA-AFGC, 2002. Ultra High Performance Fiber Reinforced Concretes. Interim Recommendations..
- 30 Soranakom, C. and Mobasher, B., 2007. Closed-Form Moment-Curvature Expressions for Homogenized Fiber-  
31 Reinforced Concrete. *ACI Materials Journal*, 104(4): 351-359.
- 32 Soranakom, C. and Mobasher, B., 2008. Correlation of tensile and flexural responses of strain softening and strain  
33 hardening cement composites. *Cement & Concrete Composites*, 30(6): 465-477.
- 34 Spasojevic, A., 2008. Structural Implication of Ultra High Performance Fibre Reinforced Concrete in Bridge Design. *PhD-*  
35 *Thesis, École Polytechnique Fédérale de Lausanne*, April.
- 36 Tailhan, J.-L., Rossi, P. & Parant, E., 2004. Inverse Numerical Approach to Determine the Uniaxial Tensile Behaviour of  
37 a Stress Hardening Cement Composite From its Bending Behaviour. *6th RILEM Symposium on Fibre-Reinforced*  
38 *Concretes (FRC) - BEFIB 2004*, 20-22 September. pp. 913-924.
- 39 Tailhan, J.-L., Boulay, C., Rossi, P. 2012. Tensile and bending behaviour of a strain hardening cement-based composite:  
40 Experimental and numerical analysis. *Cement & Concrete Composites*, Vol. 34 (2), pp. 166-171.
- 41 Walraven, J., 2012. On the way to international design recommendations for Ultra High Performance Fibre Reinforced  
42 Concrete. *Proceedings of the 3rd International Symposium on UHPC and Nanotechnology for High Performance*  
43 *Construction Materials*, 7-9 March. pp. 51-58.
- 44 Wille, K., El-Tawil, S., Naaman, A.E. Properties of strain hardening ultra high performance fiber reinforced concrete  
45 (UHP-FRC) under direct tensile loading. *Cement & Concrete Composites*. Vol. 48. 2014. pp. 53- 66.

1  
2  
3  
4  
5  
6  
7  
8  
9  
10  
11  
12  
13  
14  
15  
16  
17  
18  
19  
20  
21  
22  
23  
24  
25  
26  
27  
28  
29  
30  
31  
32  
33  
34  
35  
36  
37  
38  
39  
40  
41  
42  
43  
44  
45  
46  
47  
48  
49  
50  
51  
52  
53  
54  
55  
56  
57  
58  
59  
60  
61  
62  
63  
64  
65



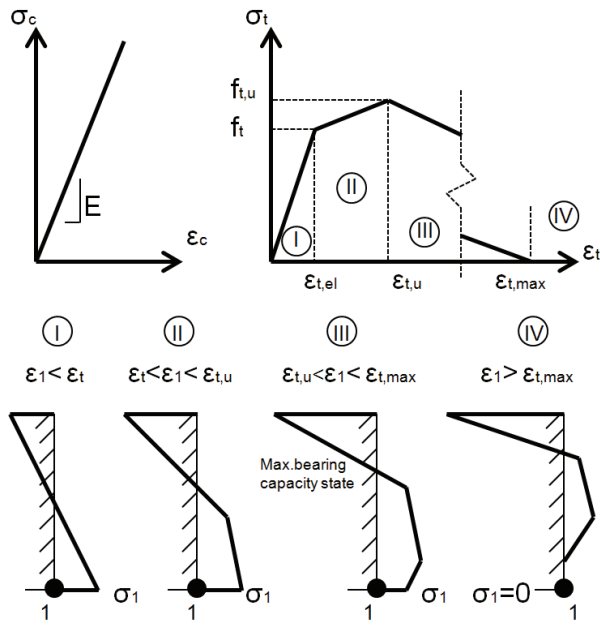


Figure 1. The  $\sigma$ - $\epsilon$  law in both compression and tension. Cross-sectional stress distribution for the different stages.

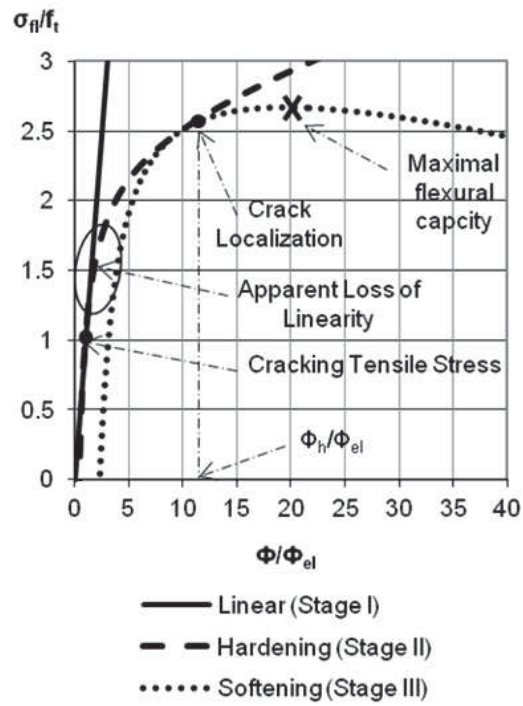


Figure 2. Normalised moment-curvature curve for typical UHPFRC with a rectangular cross-section.  $f_t = 9 \text{ MPa}$ ;  $f_{t,u} = 10 \text{ MPa}$ ;  $\varepsilon_{t,u} = 0.25\%$ ;  $\varepsilon_{t,max} = 3.4\%$ ;  $E=50 \text{ GPa}$ ;  $b=h=0.1 \text{ m}$ .

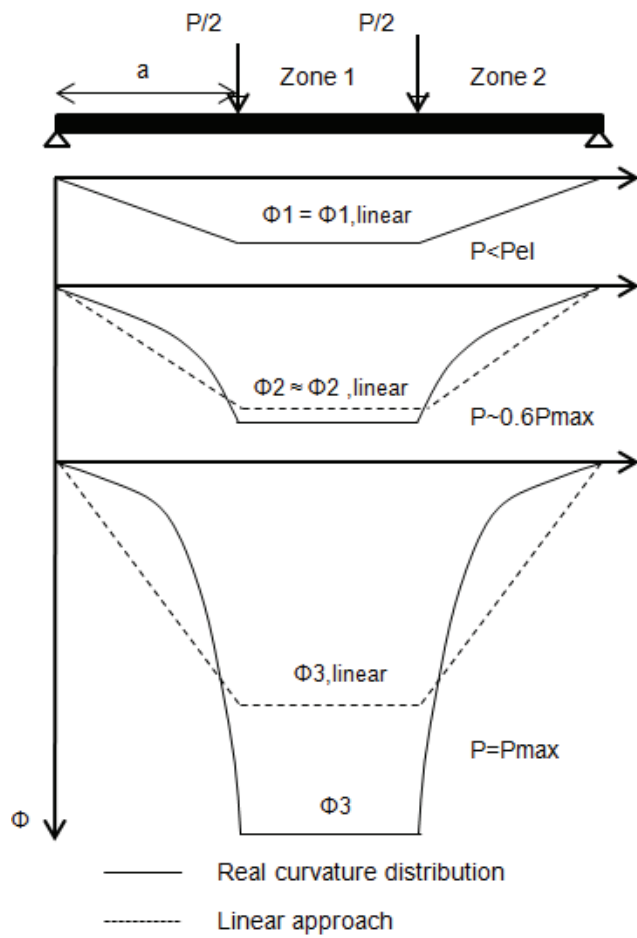


Figure 3. Qualitative comparison between the real curvature distribution and the linear approach for different loading steps

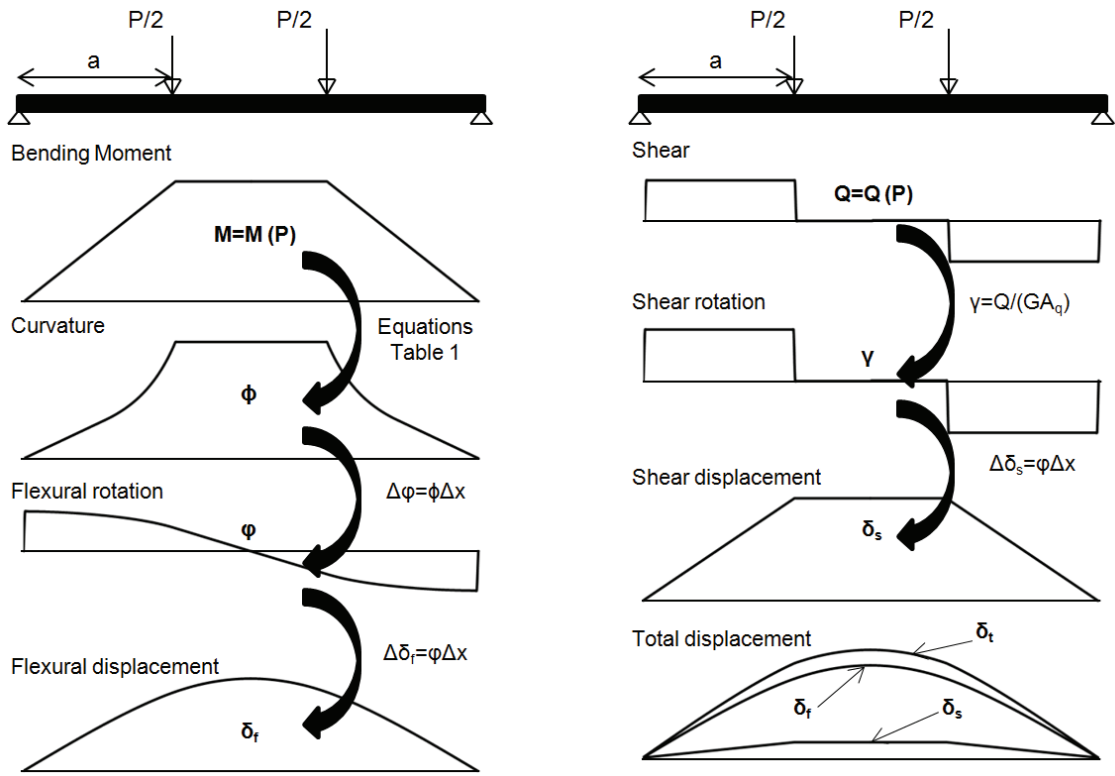


Figure 4. Procedure to obtain the load-displacement load up to maximum load due to the flexural and shear forces in a FPBT

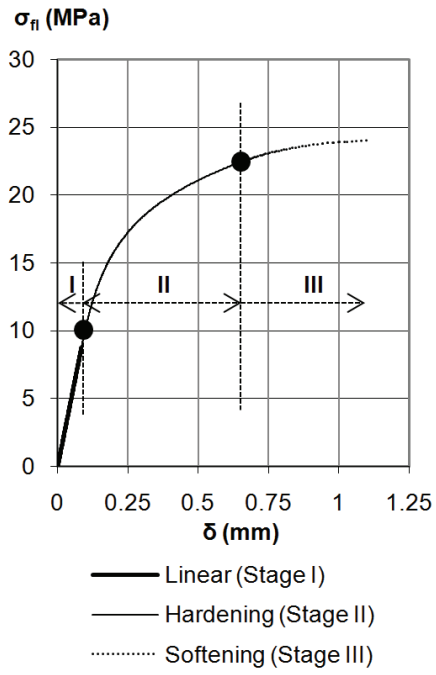


Figure 5. The numerical load-deflection curve at mid-span for a prismatic 100x100x450mm FPBT.  $f_t = 9 \text{ MPa}$ ;  $f_{t,u} = 10 \text{ MPa}$ ;  $\varepsilon_{t,u} = 0.25\%$ ;  $\varepsilon_{t,max} = 3.4\%$ ;  $E = 50 \text{ GPa}$ .

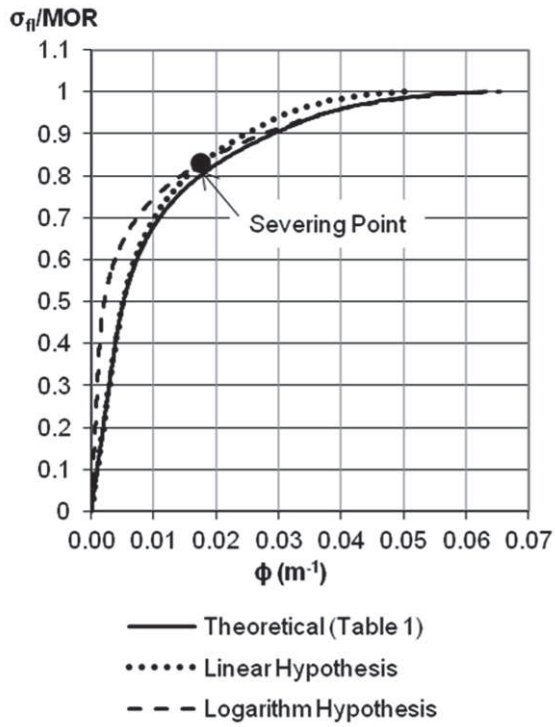


Figure 6. The load-average curvature at mid-span for a prismatic 100x100x450mm FPBT.  $f_t = 9$  MPa;  $f_{t,u} = 10$  MPa;  $\epsilon_{t,u} = 0.25\%$ ;  $\epsilon_{t,max} = 3.4\%$ ;  $E=50$  GPa.

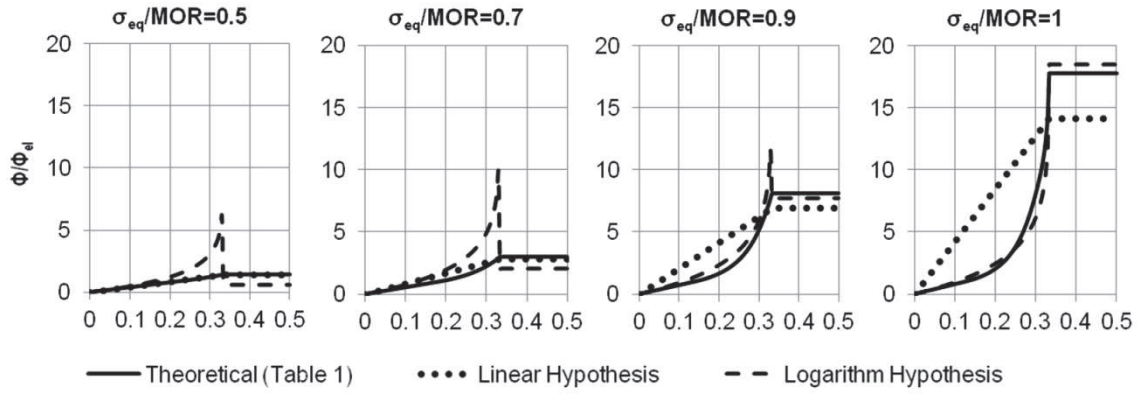


Figure 7. Curvature distribution along the half-length beam for several loading steps using the different hypothesis suggested.  $f_t = 9 \text{ MPa}$ ;  $f_{t,u} = 10 \text{ MPa}$ ;  $\epsilon_{t,u} = 0.25\%$ ;  $\epsilon_{t,max} = 3.4\%$ ;  $E=50 \text{ GPa}$ ,  $b=0.1\text{m}$ ;  $h=0.1\text{m}$ ;  $L=0.45\text{m}$ ;  $a=0.15\text{m}$

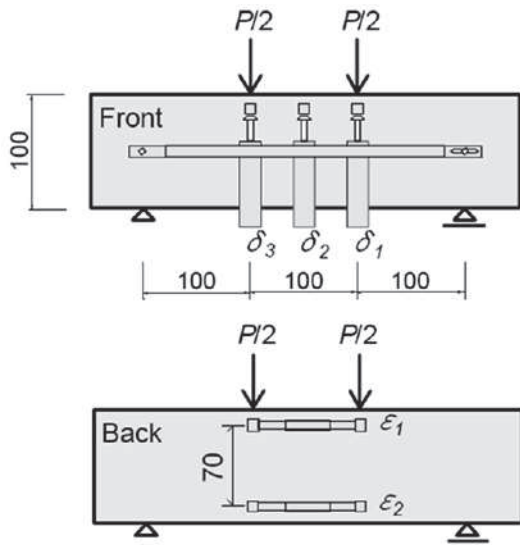


Figure 8. The FPBT configuration carried out by Kanakubo

1  
2  
3  
4  
5  
6  
7  
8  
9  
10  
11  
12  
13  
14  
15  
16  
17  
18  
19  
20  
21  
22  
23  
24  
25  
26  
27  
28  
29  
30  
31  
32  
33  
34  
35  
36  
37  
38  
39  
40  
41  
42  
43  
44  
45  
46  
47  
48  
49  
50  
51  
52  
53  
54  
55  
56  
57  
58  
59  
60  
61  
62  
63  
64  
65



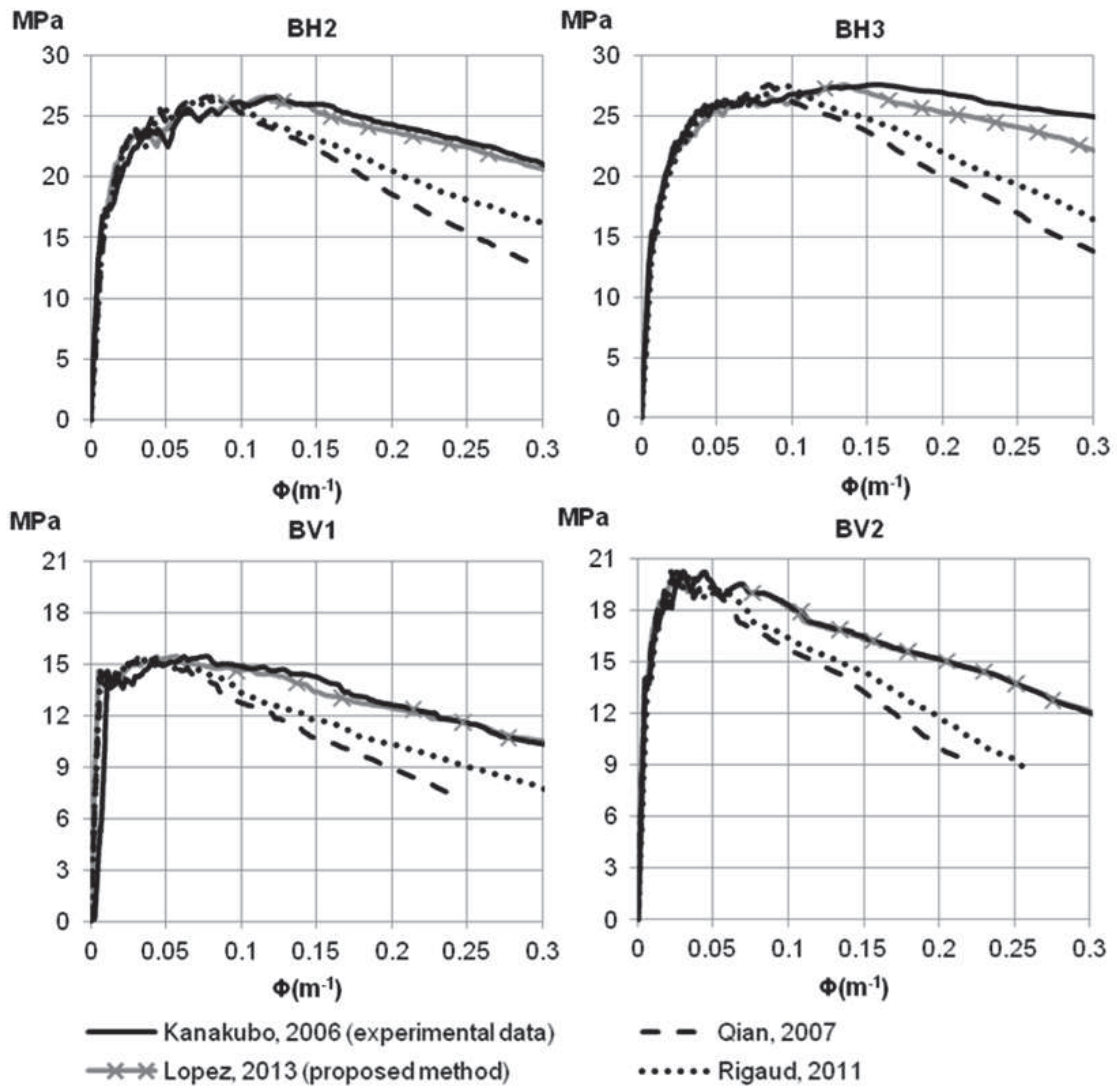


Figure 9. The  $\delta$  to  $\Phi$  transformation using the Qian, Rigaud and Lopez methods and their comparison with the experimental results in the BH1, BH2, BV1 and BV2 specimens

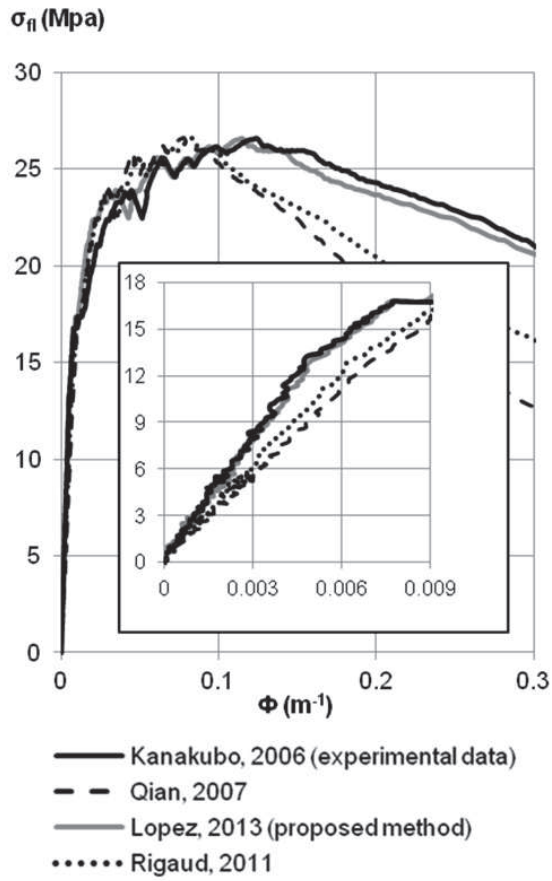


Figure 10. The comparison made of the Qian, Rigaud and Lopez methods with the experimental results for the BH-2 specimen.

1  
2  
3  
4  
5  
6  
7  
8  
9  
10  
11  
12  
13  
14  
15  
16  
17  
18  
19  
20  
21  
22  
23  
24  
25  
26  
27  
28  
29  
30  
31  
32  
33  
34  
35  
36  
37  
38  
39  
40  
41  
42  
43  
44  
45  
46  
47  
48  
49  
50  
51  
52  
53  
54  
55  
56  
57  
58  
59  
60  
61  
62  
63  
64  
65

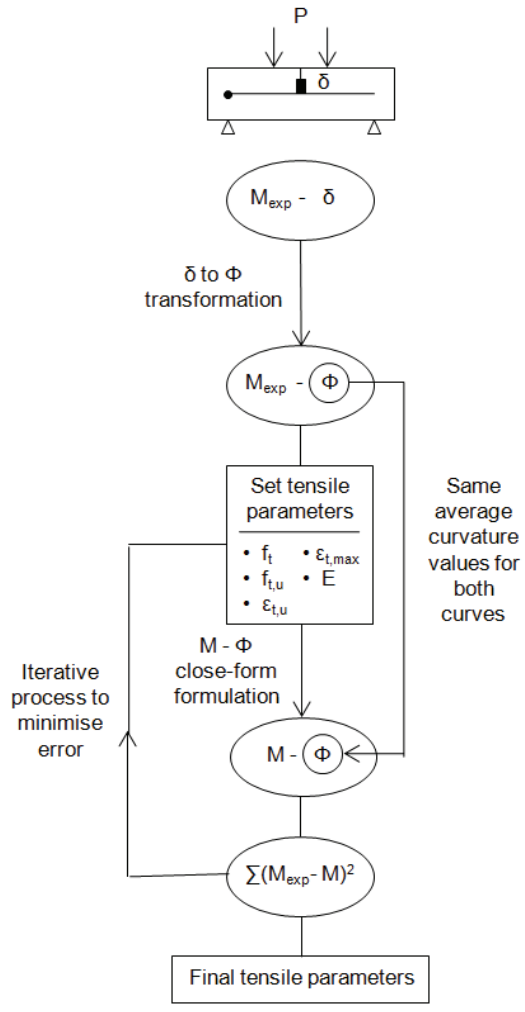


Figure 11. Scheme for the inverse analysis procedure

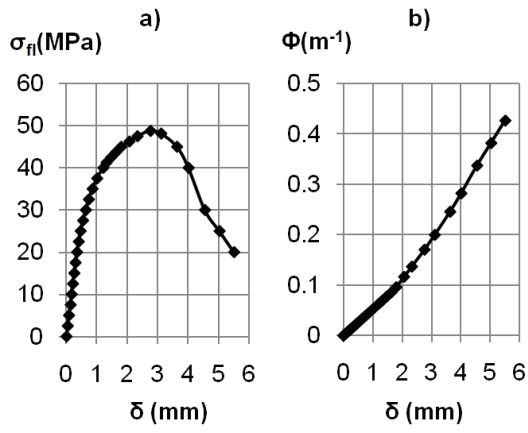
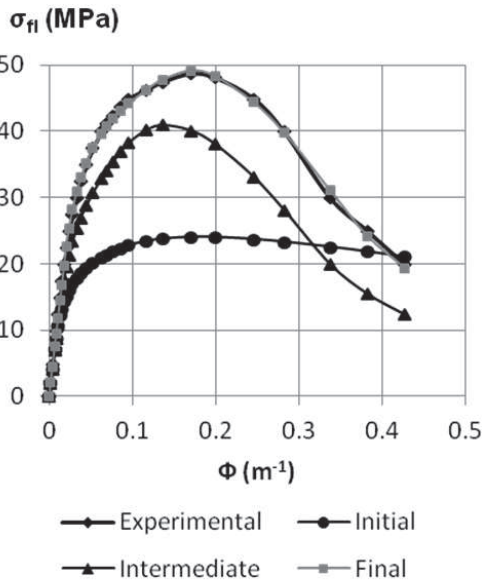


Figure 12. a) Average  $\sigma_{fi}$ - $\delta$  b) The  $\delta$  to  $\Phi$  transformation for the FPBT

1  
2  
3  
4  
5  
6  
7  
8  
9  
10  
11  
12  
13  
14  
15  
16  
17  
18  
19  
20  
21  
22  
23  
24  
25  
26  
27  
28  
29  
30  
31  
32  
33  
34  
35  
36  
37  
38  
39  
40  
41  
42  
43  
44  
45  
46  
47  
48  
49  
50  
51  
52  
53  
54  
55  
56  
57  
58  
59  
60  
61  
62  
63  
64  
65



Iteration	E (MPa)	f <sub>t</sub> (MPa)	f <sub>t,u</sub> (MPa)	ε <sub>t,u</sub>	ε <sub>t,max</sub>	Sum of residual squares (MPa <sup>2</sup> )
Initial	50000	9.0	10.0	0.0025	0.034	6394.1
-	54000	15.0	20.0	0.0025	0.010	1124.2
Final	54707	20.2	21.4	0.0045	0.012	7.6

Figure 13. The inverse analysis results for the initial, an intermediate iteration

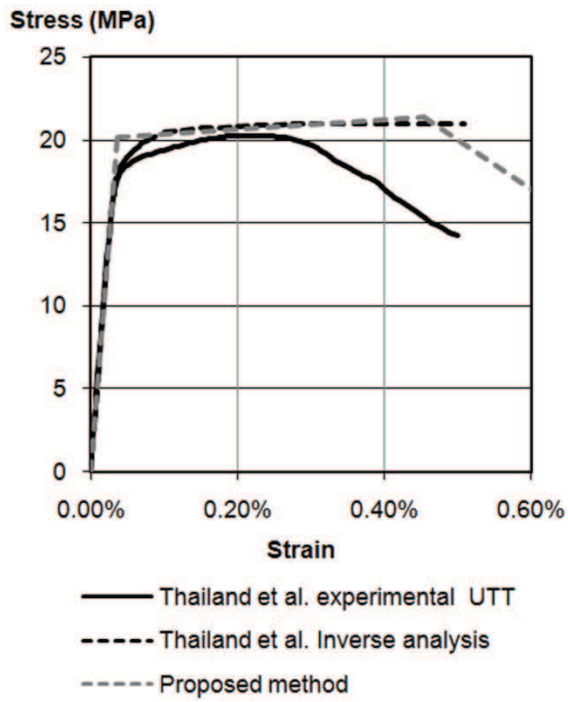


Figure 14. The constitutive tensile law from the inverse analysis

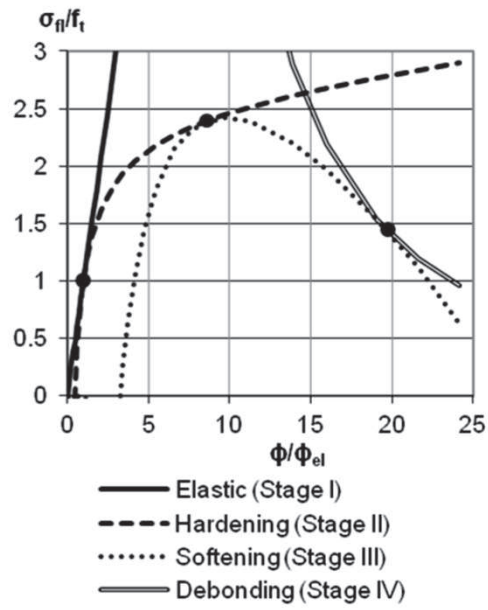


Figure 15. The normalised moment-curvature curve for the inverse analysis  $\sigma$ - $\epsilon$  law

Table 1. The close form M- $\phi$  formulation suggested for a UHPFRC rectangular cross-sectional shape

	$\phi$ Intervals	$M(\phi)$
Stage I $\phi \leq \phi_{el}$	$\phi_{el} = \frac{2f_t}{Eh}$	$M(\phi) = \frac{bh^3}{12} E\phi$
Stage II $\phi_{el} \leq \phi$ $\phi \leq \phi_h$	$\phi_h = \frac{f_t h \alpha + f_t h B_{1h}}{Eh^2}$ $B_{1h} = \sqrt{\alpha + (\alpha - 1)\gamma}$	$M(\phi) = \frac{bh}{6E(\alpha - \gamma)^2 \phi} [A_{1h}\phi^2 + A_{2h}C_{1h} + Eh\phi(A_{3h} + A_{4h}C_{1h})]$ $A_{1h} = 2E^2h^2(\gamma - 1)(\alpha + \gamma - 2)$ $A_{2h} = 2f_t(\alpha - 1)(\gamma - \alpha)$ $A_{3h} = 3f_t(\alpha - \gamma)(\alpha + \gamma - 2)$ $A_{4h} = 4(\alpha + \gamma - \alpha\gamma - 1)$ $C_{1h} = \sqrt{\frac{Eh\phi[2f_t(\alpha - \gamma) + Eh(\gamma - 1)\phi]}{\alpha - 1}}$
Stage III $\phi_h \leq \phi$ $\phi \leq \phi_s$	$\phi_s = \frac{f_t h \beta + f_t h B_{1s}}{Eh^2}$ $B_{1s} = \sqrt{\alpha + (\beta - 1)\gamma}$	$M(\phi) = \frac{b}{6E^2(\beta - \alpha + \gamma)^2 \phi^2} [A_{1s}A_{2s} + A_{3s}C_{1s} + C_{2s} + C_{3s}]$ $A_{1s} = f_t^3(\alpha - \gamma)(\alpha - \beta + \gamma(\beta - 1))$ $A_{2s} = (\alpha + 1)(\alpha - \beta) - \gamma(\alpha - 2\beta + 1)$ $A_{3s} = 2f_t^2(\alpha - \beta)(\alpha - \gamma)(\alpha - \beta + (\beta - 1)\gamma)$ $C_{1s} = \sqrt{\frac{f_t^2(\alpha - \gamma)(\alpha - \beta + (\beta - 1)\gamma) - 2Ef_t h \beta \gamma \phi + E^2 h^2 \gamma \phi^2}{\alpha - \beta}}$ $C_{2s} = Ef_t h \beta \gamma \phi (2(\alpha - \beta)C_{1s} - 3Eh\phi(\alpha - \beta + \gamma))$ $C_{3s} = 2E^2 h^2 \gamma \phi^2 (Eh(\alpha - \beta + \gamma)\phi + 2(\beta - \alpha)C_{1s})$
Stage IV $\phi_s \leq \phi$	-	$M(\phi) = \frac{bf_t^3}{6E^2 \phi^2} [A_{1u} + A_{2u}]$ $A_{1u} = 2(\alpha + (\beta - 1)\gamma)^{3/2}$ $A_{2u} = \alpha + \alpha^2 + (\beta - 1)(\alpha + \beta + 1)\gamma$

1  
2  
3  
4  
5  
6  
7  
8  
9  
10  
11  
12  
13  
14  
15  
16  
17  
18  
19  
20  
21  
22  
23  
24  
25  
26  
27  
28  
29  
30  
31  
32  
33  
34  
35  
36  
37  
38  
39  
40  
41  
42  
43  
44  
45  
46  
47  
48  
49  
50  
51  
52  
53  
54  
55  
56  
57  
58  
59  
60  
61  
62  
63  
64  
65



Table 2. Deviation in the curvature determination by the different load-curvature methods

	Deviation (‰)			
	BH-2	BH-3	BV-1	BV-2
Lopez, 2012	0.267	0.712	0.279	0.009
Rigaud, 2011	2.774	4.289	2.548	1.871
Qian, 2007	4.841	6.115	4.654	2.944

1  
2  
3  
4  
5  
6  
7  
8  
9  
10  
11  
12  
13  
14  
15  
16  
17  
18  
19  
20  
21  
22  
23  
24  
25  
26  
27  
28  
29  
30  
31  
32  
33  
34  
35  
36  
37  
38  
39  
40  
41  
42  
43  
44  
45  
46  
47  
48  
49  
50  
51  
52  
53  
54  
55  
56  
57  
58  
59  
60  
61  
62  
63  
64  
65

- 1 Figure 1. The  $\sigma$ - $\varepsilon$  law in both compression and tension. Cross-sectional stress distribution for the different stages.
- 2 Figure 2. Normalised moment-curvature curve for typical UHPFRC with a rectangular cross-section.  $f_t = 9 \text{ MPa}$ ;  $f_{t,u} = 10$   
3  $\text{MPa}$ ;  $\varepsilon_{t,u} = 0.25\%$ ;  $\varepsilon_{t,max} = 3.4\%$ ;  $E=50 \text{ GPa}$ ;  $b=h=0.1 \text{ m}$ .
- 4 Figure 3. Qualitative comparison between the real curvature distribution and the linear approach for different loading  
5 steps
- 6
- 7 Figure 4. Procedure to obtain the load-displacement load up to maximum load due to the flexural and shear forces in a  
8 FPBT
- 9
- 10 Figure 5. The numerical load-deflection curve at mid-span for a prismatic 100x100x450mm FPBT.  $f_t = 9 \text{ MPa}$ ;  $f_{t,u} = 10$   
11  $\text{MPa}$ ;  $\varepsilon_{t,u} = 0.25\%$ ;  $\varepsilon_{t,max} = 3.4\%$ ;  $E=50 \text{ GPa}$ .
- 12 Figure 6. The load-average curvature at mid-span for a prismatic 100x100x450mm FPBT.  $f_t = 9 \text{ MPa}$ ;  $f_{t,u} = 10 \text{ MPa}$ ;  $\varepsilon_{t,u} =$   
13  $0.25\%$ ;  $\varepsilon_{t,max} = 3.4\%$ ;  $E=50 \text{ GPa}$ .
- 14
- 15 Figure 7. Curvature distribution along the half-length beam for several loading steps using the different hypothesis  
16 suggested.  $f_t = 9 \text{ MPa}$ ;  $f_{t,u} = 10 \text{ MPa}$ ;  $\varepsilon_{t,u} = 0.25\%$ ;  $\varepsilon_{t,max} = 3.4\%$ ;  $E=50 \text{ GPa}$ ,  $b=0.1\text{m}$ ;  $h=0.1\text{m}$ ;  $L=0.45\text{m}$ ;  $a=0.15\text{m}$
- 17
- 18 Figure 8. The FPBT configuration carried out by Kanakubo
- 19
- 20 Figure 9. The  $\delta$  to  $\Phi$  transformation using the Qian, Rigaud and Lopez methods and their comparison with the  
21 experimental results in the BH1, BH2, BV1 and BV2 specimens
- 22
- 23 Figure 10. The comparison made of the Qian, Rigaud and Lopez methods with the experimental results for the BH-2  
24 specimen.
- 25
- 26 Figure 11. Scheme for the inverse analysis procedure
- 27
- 28 Figure 12. a) Average  $\sigma_{fl}$ - $\delta$  b) The  $\delta$  to  $\Phi$  transformation for the FPBT
- 29
- 30 Figure 13. The inverse analysis results for the initial, an intermediate iteration
- 31
- 32 Figure 14. The constitutive tensile law from the inverse analysis
- 33
- 34 Figure 15. The normalised moment-curvature curve for the inverse analysis  $\sigma$ - $\varepsilon$  law
- 35
- 36
- 37
- 38
- 39
- 40
- 41
- 42
- 43
- 44
- 45
- 46
- 47
- 48
- 49
- 50
- 51
- 52
- 53
- 54
- 55
- 56
- 57
- 58
- 59
- 60
- 61
- 62
- 63
- 64
- 65

List of Tables

[Click here to download attachment to manuscript: List of tables.docx](#)

[Click here to view linked References](#)

Table 1. The close form M- $\phi$  formulation suggested for a UHPFRC rectangular cross-sectional shape

Table 2. Deviation in the curvature determination by the different load-curvature methods

- 1
- 2
- 3
- 4
- 5
- 6
- 7
- 8
- 9
- 10
- 11
- 12
- 13
- 14
- 15
- 16
- 17
- 18
- 19
- 20
- 21
- 22
- 23
- 24
- 25
- 26
- 27
- 28
- 29
- 30
- 31
- 32
- 33
- 34
- 35
- 36
- 37
- 38
- 39
- 40
- 41
- 42
- 43
- 44
- 45
- 46
- 47
- 48
- 49
- 50
- 51
- 52
- 53
- 54
- 55
- 56
- 57
- 58
- 59
- 60
- 61
- 62
- 63
- 64
- 65